ISSN 1005-0302
Volume 34 Number 2 2018

Journal of MATERIALS SCIENCE & TECHNOLOGY

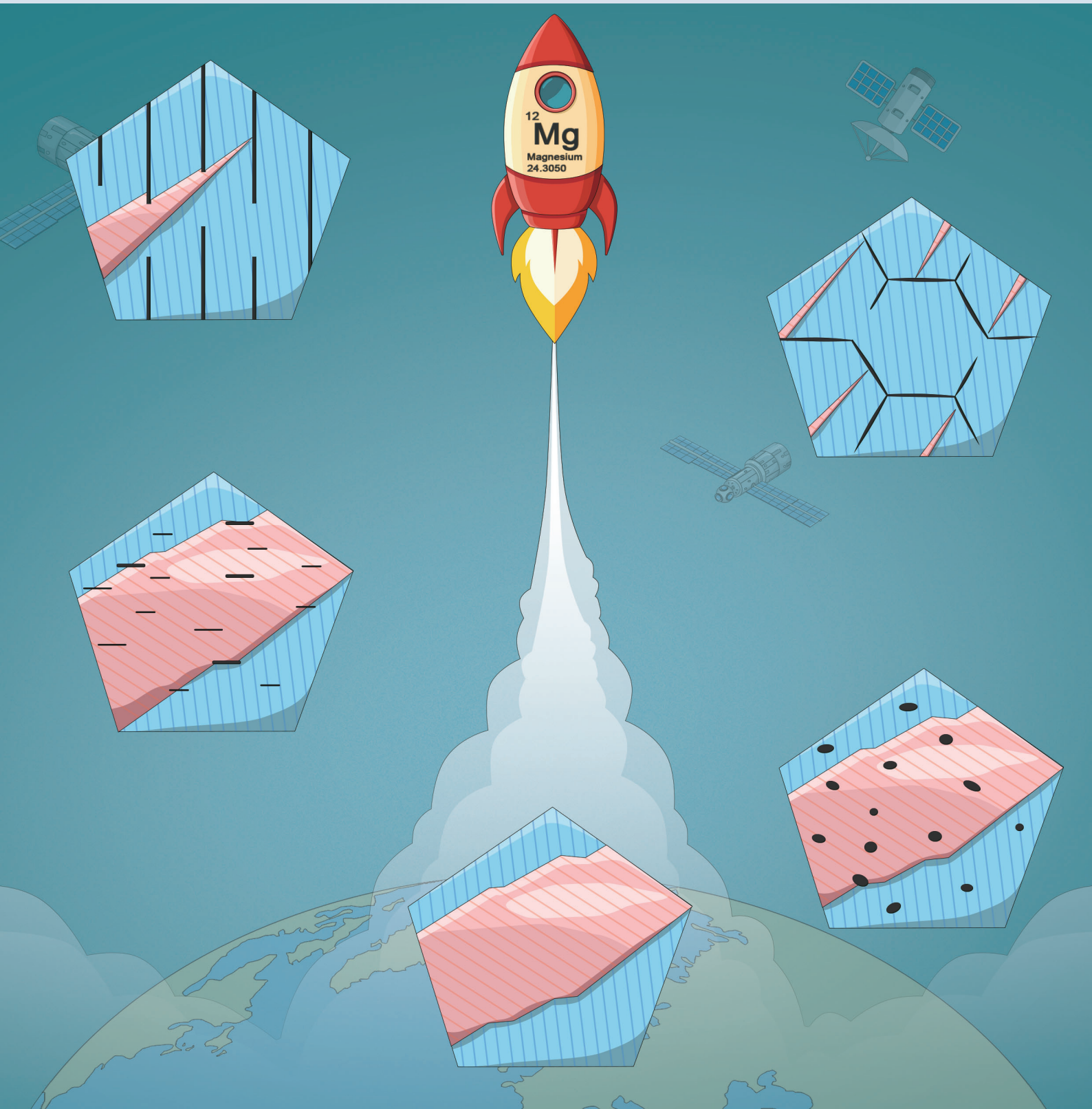

Journal of Materials Science & Technology 34 (2018) 1061–1066

Contents lists available at ScienceDirect

Journal of Materials Science & Technology

journal homepage: www.jmst.org

Insight from *in situ* microscopy into which precipitate morphology can enable high strength in magnesium alloys

Bo-Yu Liu[a,1], Nan Yang[a,1], Jian Wang[b], Matthew Barnett[c], Yun-Chang Xin[d], Di Wu[e], Ren-Long Xin[d], Bin Li[f], R. Lakshmi Narayan[a,g], Jian-Feng Nie[h], Ju Li[a,i], Evan Ma[a,j,*], Zhi-Wei Shan[a,*]

[a] *Center for Advancing Materials Performance from the Nanoscale (CAMP-Nano) & Hysitron Applied Research Center in China (HARCC), State Key Laboratory for Mechanical Behavior of Materials, Xi'an Jiaotong University, Xi'an 710049, People's Republic of China*
[b] *Mechanical and Materials Engineering, University of Nebraska-Lincoln, Lincoln, NE 68588, USA*
[c] *Institute for Frontier Materials, Deakin University, Geelong, Victoria 3216, Australia*
[d] *College of Materials Science and Engineering, Chongqing University, Chongqing 400045, People's Republic of China*
[e] *Institute of Metal Research, Chinese Academy of Sciences, Shenyang 110016, People's Republic of China*
[f] *Department of Chemical and Materials Engineering, University of Nevada, Reno, USA*
[g] *Department of Materials Science and Engineering, Carnegie Mellon University, Pittsburgh, PA 15213, USA*
[h] *Department of Materials Science and Engineering, Monash University, Melbourne, Victoria 3800, Australia*
[i] *Department of Nuclear Science and Engineering and Department of Materials Science and Engineering, Massachusetts Institute of Technology, 77 Massachusetts Avenue, Cambridge, MA 02139, USA*
[j] *Department of Materials Science and Engineering, Johns Hopkins University, Baltimore, MD 21218, USA*

ARTICLE INFO

Article history:
Received 2 January 2018
Received in revised form 12 January 2018
Accepted 18 January 2018
Available online 14 February 2018

Keywords:
Precipitate selection criterion
In-situ TEM
Mg alloy
Mechanical property
Deformation twinning

ABSTRACT

Magnesium alloys, while boasting light weight, suffer from a major drawback in their relatively low strength. Identifying the microstructural features that are most effective in strengthening is therefore a pressing challenge. Deformation twinning often mediates plastic yielding in magnesium alloys. Unfortunately, due to the complexity involved in the twinning mechanism and twin-precipitate interactions, the optimal precipitate morphology that can best impede twinning has yet to be singled out. Based on the understanding of twinning mechanism in magnesium alloys, here we propose that the lamellar precipitates or the network of plate-shaped precipitates are most effective in suppressing deformation twinning. This has been verified through quantitative *in situ* tests inside a transmission electron microscope on a series of magnesium alloys containing precipitates with different morphology. The insight gained is expected to have general implications for strengthening strategies and alloy design.

1. Introduction

Lightweight magnesium (Mg) alloys are being actively pursued for their energy saving potential in fuel intensive transport [1,2]. However, the low strength of Mg alloys seriously hampers their broad applications. The idea of age hardening, inspired by success with Al alloys [3], has been widely applied to Mg alloys by introducing precipitates to enhance the strength. However, the strengthening effect is unsatisfactory [4] (Fig. S1). Different from Al alloys whose plasticity is governed exclusively by dislocation slips, yielding of Mg is usually subsidized by both dislocation slips on basal plane and deformation twinning (DT) on $\{10\bar{1}2\}$ plane (Fig. S2) [5]. The suppression of both basal slip and $\{10\bar{1}2\}$ DT is necessary in strengthening Mg alloys. For basal slips, the resistance from precipitates can be well quantified by Orowan model [6–8] and the strengthening effect is reliable [8–13]. However, from the experimental point of view, a consensus has yet to be reached whether the $\{10\bar{1}2\}$ DT can be effectively suppressed by precipitates [9–15] (Table S1). Although a few microscopy studies suggested that twin

* Corresponding authors at: Center for Advancing Materials Performance from the Nanoscale (CAMP-Nano) & Hysitron Applied Research Center in China (HARCC), State Key Laboratory for Mechanical Behavior of Materials, Xi'an Jiaotong University, Xi'an 710049, People's Republic of China.
E-mail addresses: ema.mse.jhu@gmail.com (E. Ma), zwshan@xjtu.edu.cn (Z.-W. Shan).
[1] These authors contributed equally to this work.

https://doi.org/10.1016/j.jmst.2018.01.017
1005-0302/

can be arrested by precipitates [16–19], they could not tell if twin can move again to pass through those precipitates, and how much stress increase would be needed for that to occur. The theoretically predicted best precipitates for blocking DT are prismatic plates [4,20], but DT can not be reduced by such precipitates in some experiments [10,14]. With readily activated $\{10\bar{1}2\}$ DT, Mg alloys still suffer from low strength [21]. Therefore, an effective precipitate morphology that can impede $\{10\bar{1}2\}$ DT to a great degree is pressingly needed for developing high strength Mg alloys.

The present work was inspired by an atomistic understanding of twinning mechanism in Mg. $\{10\bar{1}2\}$ DT can grow through the migration of basal-prismatic interfaces (BP) [22–25] and the twin is then not restricted on the $\{10\bar{1}2\}$ plane [26–28]. This facilitates the growth of $\{10\bar{1}2\}$ twin in a flexible manner (with liquid-like characteristics): when a part of the twin is pinned by precipitates, the other parts can still migrate via BP migration. A hint of this phenomenon is that the twin boundary is always curved when it intersects with precipitates [7,16–19,29,30]. As such, we hypothesize that if the precipitate entails a high aspect ratio (like a wall), or the precipitates connect with each other to form a three-dimensional network, the expanding twin would have a hard time bypassing or engulfing such an obstacle. When twinning becomes difficult, non-basal dislocation slips that originally do not come into play would necessarily become activated (Fig. S3). Fig. 1 outlines this proposed strategy for the selection of precipitate morphology in Mg alloys.

2. Material and methods

It is however difficult to validate the strategy as proposed in Fig. 1, using conventional experimental methods. This is because in bulk samples there are multiple obscuring factors that would make the result ambiguous, including the simultaneous activation of multiple deformation modes that interact (DT, basal and non-basal slips) [31], varying grain size and crystal orientations of different proportions, non-uniform spatial distribution of precipitates, as well as the frequent occurrence of detwinning. In order to pinpoint the obstructing effect of each type of precipitate morphology on $\{10\bar{1}2\}$ DT, we tested inside a transmission electron microscope (TEM) a series of Mg alloys, each being a microscale sample containing only a specific morphology. Since it is difficult to obtain all morphologies for a specific precipitate phase at one alloy composition, we used several alloys, including Mg-Al (AZ31), Mg-Zn (ZK60 and Z6), Mg-Y-Nd (WE54) and Mg-Gd-Y-Zn (GWZ931), to cover the whole range of shape of precipitates, such as particles, rods, plates and lamellar precipitates (Fig. 2). In order to exclude the effect of different solute species, precipitate phase/composition and lattice constant (e.g. c/a ratio), whenever possible we directly compared the twinning behavior and mechanical data from a same alloy system. To avoid the interference from basal slips, the compression loading axis for all the tested samples is aligned in parallel with the basal plane to ensure the dominancy of $\{10\bar{1}2\}$ DT.

3. Results and discussion

3.1. Microscopy observations

As shown in Fig. 2(a) and (b), and (Supplementary Materials) S4-S6, DT in pillars with dispersed particles, rods or nano plates behaved similarly to that in pure Mg pillars: a twin formed at the top of the pillar and finally engulfed almost the entire pillar. The densely distributed precipitates neither blocked twin growth, nor divided the twin into smaller pieces. The DT behavior was quite different when the precipitates were connected to each other. Fig. 2(c) shows a WE54 pillar where the precipitate formed a network: no twin could be detected. During compressive loading, the pillar underwent obvious plastic deformation, but the latter must be mediated by non-basal dislocation slip (see Fig. S3 for possible slip systems). This is in stark contrast to the test on another pillar containing two isolated plates fabricated from the same WE54 sample. In such a pillar, when applied stress reached a critical level, twin was nucleated and expanded towards the root part of the pillar (Fig. S7). Similar suppression of DT could also be achieved in GWZ931 pillars containing long-period-stacking-order (LPSO) lamellae (Fig. 2(d)). After this pillar was shortened along the axial direction by ~7%, only two small volumes were twinned. In contrast, in the test on another pillar containing less LPSO lamellae that was fabricated from the same GWZ931 sample, twinning still dominated the plastic deformation (Fig. S8). With the increasing volume fraction of

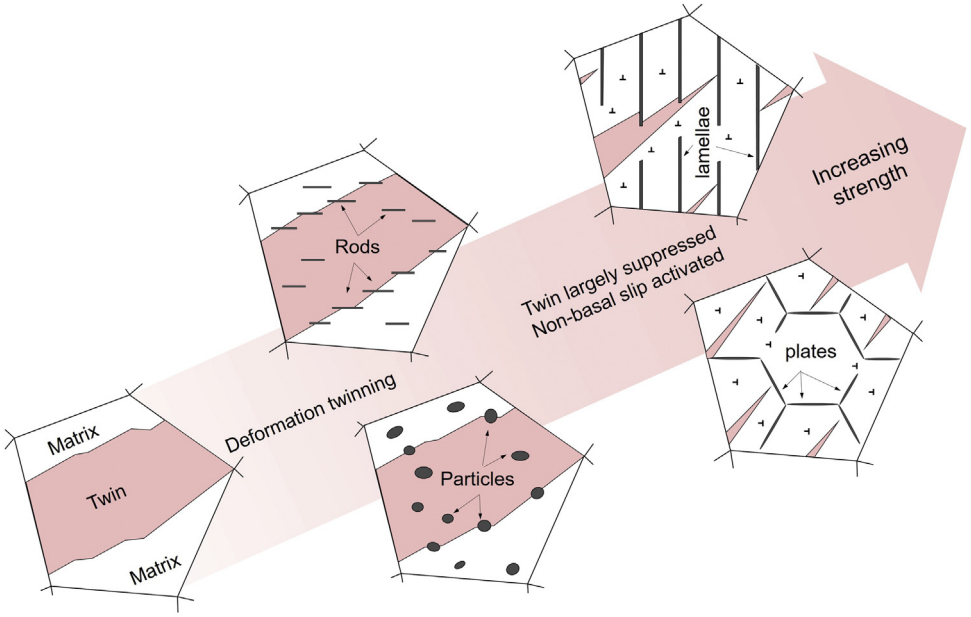

Fig 1. Criteria for precipitate morphology selection in the design of high-strength Mg alloys.

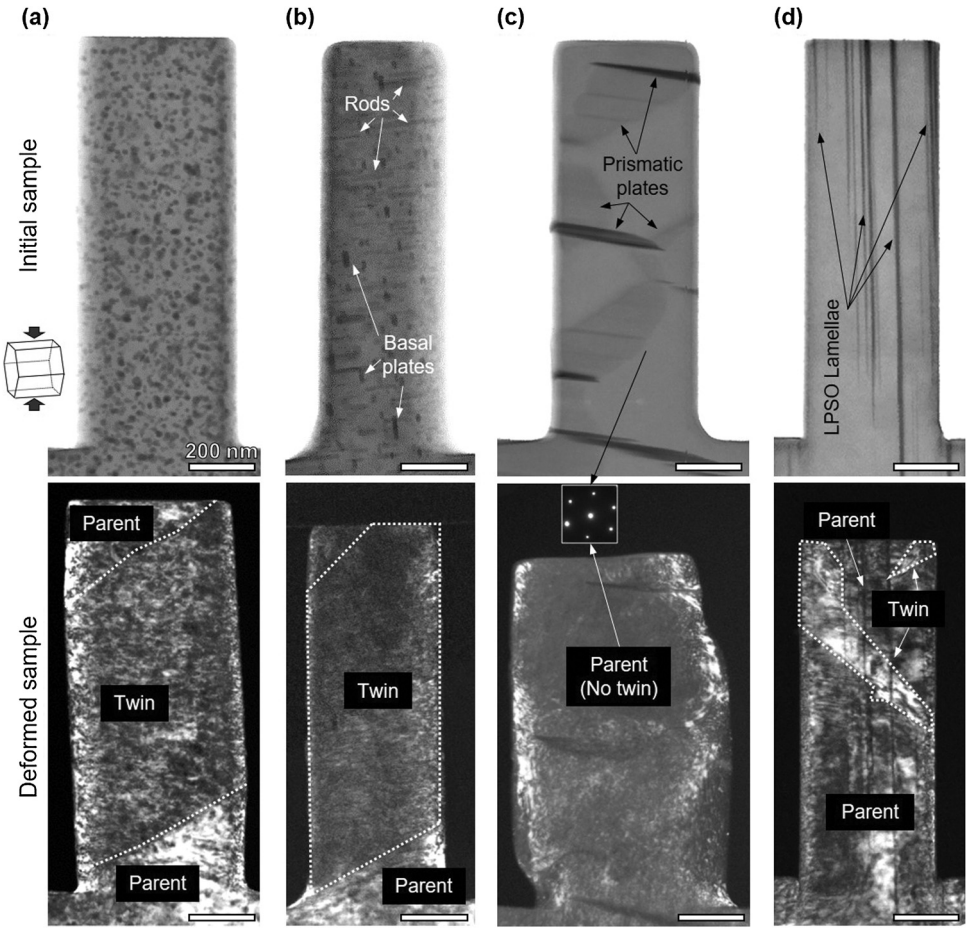

Fig. 2. In-situ TEM observation of the deformation behavior of Mg alloys with different precipitate morphology. Top row, bright field Scanning Transmission Electron Microscope (STEM) images showing initial samples. Bottom row, dark field TEM images showing deformed samples. In (a) ZK60 pillar with particles, (b) Z6 pillar with rods and a small number of nanoscale plates, almost the entire pillar is twinned. In (c) WE54 pillar with plate-network or in (d) GWZ931 pillar with LPSO lamellae, DT is significantly suppressed. Compressive loading was along the pillar axial orientation, which is parallel to the $\{0002\}$ plane (basal) of Mg. The observation (electron beam) direction is parallel to the basal plane in (a), (b), (d), and is parallel to the *c*-axis in (c). All scale bars, 200 nm.

LPSO lamellae, we found that twinning was generally reduced and finally eliminated (Fig. S9).

3.2. Mechanical responses

Next, we analyzed how precipitates influenced the measured stress-strain curves. Fig. 3(a) displays stress-strain curves of ZK60 pillar containing particles (red), Z6 pillar containing c-axis rods (blue), and pure Mg pillar (green). The curves of ZK60 and Z6 pillars exhibit a similar shape, and the flow stresses are at the same level. According to the *in situ* videos (Supplementary Video S1 and S2), in both pillars twinning set in when stress reached ~350 MPa. After that, twin thickened in a jerky way, as manifested in the stress-strain curve by several small strain bursts. From the *in situ* videos, these strain bursts and stress dropping appeared to correspond to a breaking away of the twin boundary from precipitates, reflecting the obstructing effect of precipitates on twin boundary migration. This is different from the smooth twin boundary migration in pure Mg pillars. During twin growth, the flow stress stayed at the level of ~400 MPa with no obvious work-hardening. Compared with pure Mg pillars, the yield and flow stresses of pillars containing particles or rods were improved by ~20%.

In WE54 pillars, the flow stresses were higher and the plastic flow was smoother (Fig. 3(b)). In the pillar with isolated prismatic plates (Supplementary Video S3 and Fig. S7(a)), the formation of DT was delayed to after 8% engineering strain. At this time, the corresponding stress approached ~500 MPa. In the pillar with plates that formed a network (Supplementary Video S4 and Fig. S7(b)), no twin formed and remarkable work-hardening could be observed after yielding. The peak stress was ~600 MPa (engineering strain ~10%). After that, the stress decreased, which might be related to the shearing of one plate.

High stresses could also be sustained in GWZ931 pillars (Fig. 3(c)). In the case with a few LPSO layers (Supplementary Video S5 and Fig. S8(a)), a twin formed then expanded under the stress of ~500 MPa. Very interestingly, increasing the number of LPSO layers (increasing volume fraction) was able to further suppress DT. This was accompanied by remarkable strengthening: the yield stress and flow stress reached ~620 MPa and ~700 MPa, respectively. From the *in situ* video (Supplementary Video S6 and Fig. S8(b)), only two small twins appeared. The first twin formed well beyond yielding, after ~4% engineering strain had already set in. This small twin terminated at one of the LPSO layers and did not grow further upon continued loading. Another small twin formed at ~5% strain, and grew with increasing applied strain.

3.3. Strain-component analysis

Both the visual *in situ* observations and the mechanical data indicate that the remarkable strengthening arises from the suppression of DT. To demonstrate that strengthening indeed originates from the switch in plasticity mechanism, we have carried out a "strain-

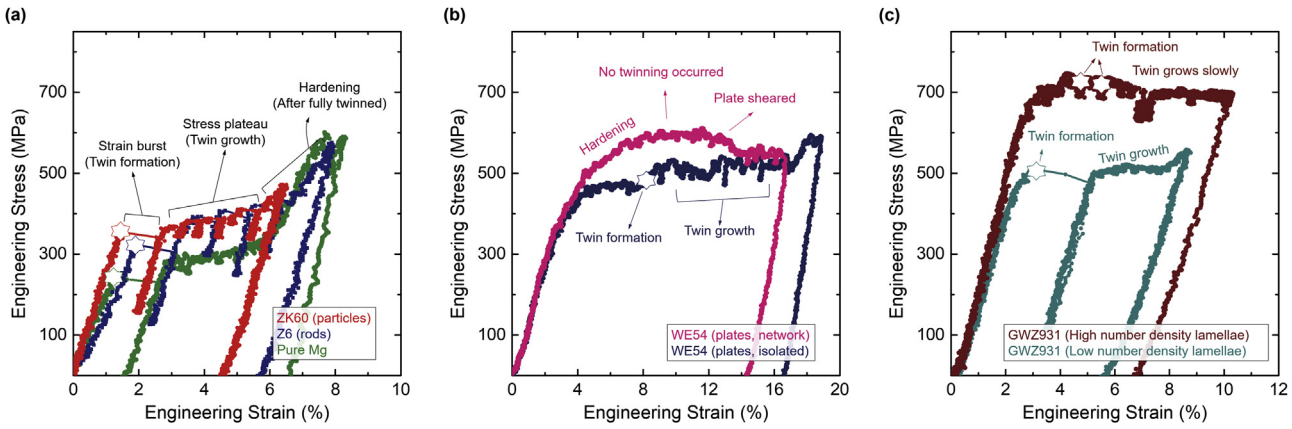

Fig. 3. Stress-strain curves of tested pillar with various precipitate morphology. (a) ZK60, Z6 and pure Mg pillar. (b) WE54 pillars. (c) GWZ931 pillars. The hexagram represents the twin formation.

component analysis" in Fig. 4, which displays the contribution of elastic strain ($\varepsilon_{elastic}$), dislocation-slip mediated strain ($\varepsilon_{dislocation}$) and twinning mediated strain (ε_{twin}) to the total engineering strain (ε_{total}) along the compression direction in the four pillars as shown in Fig. 2. All horizontal axes start from 1.5% to avoid the complex stress and strain condition when the indenter just contacts the pillar. The flow stress is seen to scale inversely with the contribution of twinning to the total plastic strain. For example, in pure Mg pillars (Supplementary Materials Fig. S10) and pillars with particles or rods (Fig. 4(a) and (b)), twinning starts at 1–2% strain and dom-

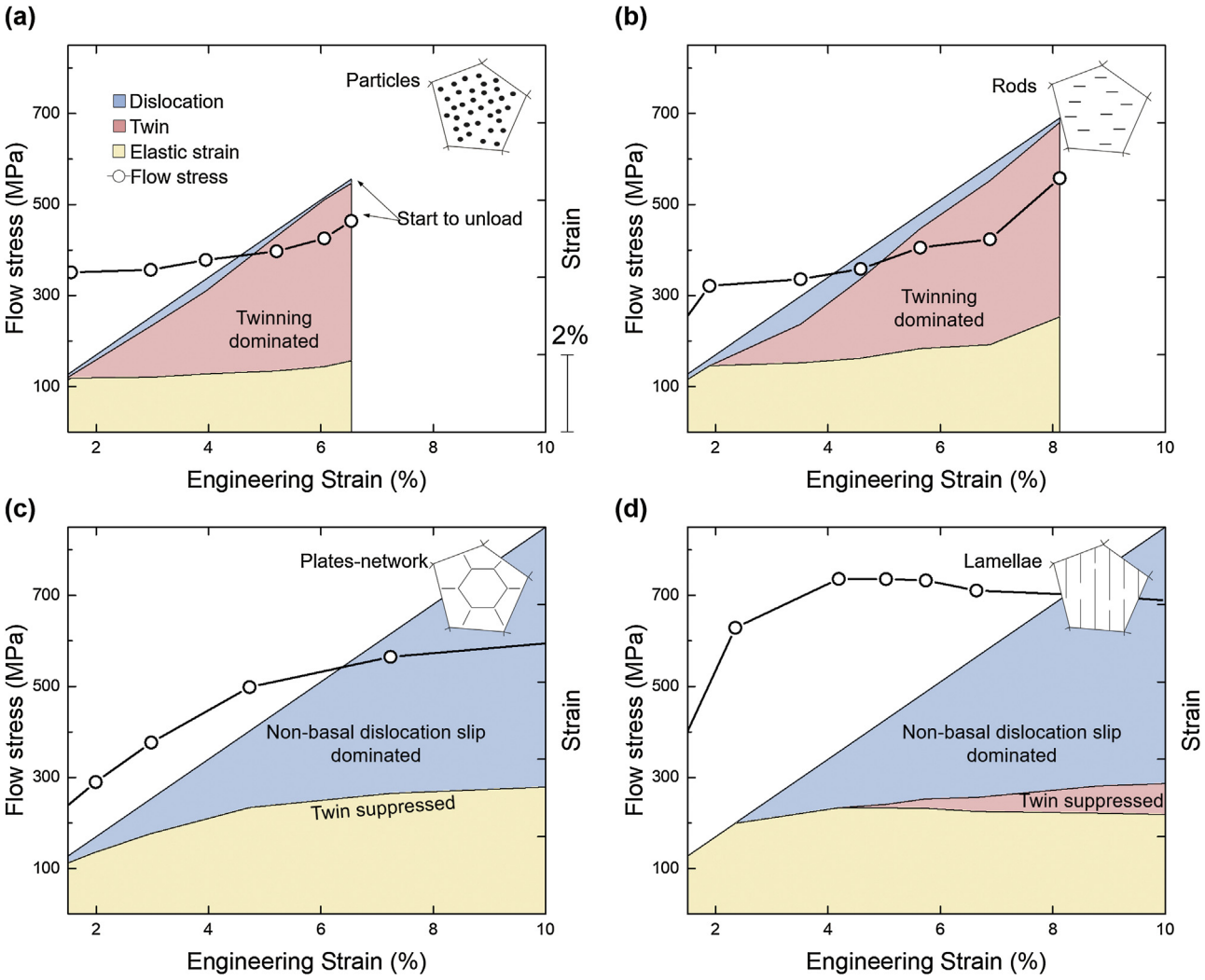

Fig. 4. Strain-component analyses demonstrating the trend that the suppression (promotion) of DT (dislocation slip) corresponds to higher strength. Diagrams showing the proportion of $\varepsilon_{elastic}$, $\varepsilon_{dislocation}$ and ε_{twin} in the ε_{total} along the programed straining process, overlapped with the flow stresses, in four tested pillars with particles (a), rods (b), plate-networks (c) and lamellae (d).

inates the plastic strain; this profuse twinning corresponds to a relatively low flow stress in a range of 250–400 MPa. It should be noted that the compressive loading direction was not always perfectly parallel to the basal plane. As a result, a small degree of basal slips is expected in the present experiments. In contrast, in the pillar with plate-network, DT was completely suppressed and dislocation slips dominated the plastic strain. The absence of twinning is tantamount to a much higher flow stress (Fig. 4(c)) and stronger strain hardening. Similarly, in the pillars with lamellar structures, only a small amount of twinning occurred after 4% strain and dislocation slip was the dominant plasticity carrier. The flow stress sustained went up to ~700 MPa (Fig. 4(d)).

3.4. Strengthening factors

The high strength obtained in our tested pillars can be attributed to the following factors: sample dimensions, solute atoms and precipitates. First, sample size effect. In accordance with the trend of "smaller is stronger [32]", the strength of micro-/nano-scale samples that have similar sizes for our pillars, was generally higher than that in bulk scale samples. However, the scale of $\sim 10^2$ nm was not small enough to eliminate the $\{10\bar{1}2\}$ DT. Twinning still dominated the plastic deformation in our pure Mg, Mg-Al and Mg-Zn pillars.

Second, solute atoms. In our experiments, because DT was still dominant in rare-earth (RE) free pillars, but suppressed in Mg-RE pillars (Mg-Y-Nd and Mg-Gd-Y-Zn), here we focused on Y, Nd and Gd. Such RE elements were found to have a strengthening effect for Mg alloys [33]. For Y, a high content of Y solutes was reported to reduce $\{10\bar{1}2\}$ DT [34]. The effect of Nd can be neglected here because they are expected to be completely consumed in forming precipitates [35]. For Gd, it has been reported that Gd dissolved in matrix couldn't obstruct the twin growth until they segregated on the twin boundary after annealing [36]. Therefore, in our WE54 and GWZ931 pillars, Y was expected to contribute to the suppression of DT. This could be one reason for the generally higher stress required for DT in Mg-RE pillars than in RE-free pillars. Nevertheless, in Mg-RE pillars, once nucleated, twin could still expand to large volume (Figs. S7(a) and S8(a)). Further suppression of DT required the optimization of precipitate morphology.

Third, precipitates. Since all WE54 pillars and GWZ931 pillars were fabricated from the same WE54 sample and GWZ931 sample, respectively, the solute species and concentration should be the same. Therefore, the change of DT behavior and strength should result from the change of precipitates only. In the WE54 pillar with two isolated prismatic plates, $\{10\bar{1}2\}$ DT could still nucleate and grow (Fig. S7(a)). The failure in suppressing $\{10\bar{1}2\}$ DT by prismatic plates was also reported in Ref. [10,14]. In contrast, in the WE54 pillar with plate-network, no $\{10\bar{1}2\}$ twin could be detected (Fig. S7(b)). Since such network structure (like a honeycomb) was only occasionally observed in local areas [37], the suppression of $\{10\bar{1}2\}$ DT was not observed in bulk WE54 alloys.

In GWZ931 pillars, the general trend is that high volume fraction of LPSO precipitates leads to less DT and higher flow stress. In the pillar shown in Fig. S9(d), there are three LPSO lamellae at left that are much thicker than the other two lamellae and all the lamellae in other pillars. In this pillar, twin was fully suppressed, and the highest strength was achieved (Fig. S9(e)). In contrast to the isolated particles, rods and plates, the LPSO lamellae have a high aspect ratio. First, this geometric configuration may provide large internal stress against the twin thickening [7,20]; Second, such wall-like barriers make it difficult for a twin to bypass or envelope, much like stopping flooding using a dam. Third, when the LPSO lamella encompasses the entire cross-section of the pillar, the Mg matrix is divided into nanoscale volumes (similar condition can also be reached by plate-networks). This imposes elastic and geometric constraints on DT. In metals with hexagonal close packed structure (e.g. Mg), DT is known to be much more grain size aware than the dislocation slip [38]. In small volumes the nucleation stress for DT would dramatically increase, giving way to dislocation slip as the dominant plastic carrier. One can expect that DT will be effectively suppressed when the spacing between each LPSO lamella is smaller enough (akin to grain refinement). Moreover, the probability of a twin being arrested will increase when the LPSO lamella possesses larger area. Therefore, LPSO lamellae with fine spacing and large area (encompasses the entire grain) could be the effective strengthening structure to reduce DT and enhance the strength of Mg alloys.

4. Conclusion

Our systematic dataset verified the proposal in Fig. 1, which inspires future designs of high strength Mg alloys. One desirable microstructure that comes to mind is the honeycomb arrangement of prismatic plates, which has been occasionally observed in local areas in Mg-Sm alloys [39] or in Mg-Y-Nd alloys [40]. Note that prismatic plates also have a strong obstructing effect on basal slips [8,10]. The next step is to understand the general conditions needed for the widespread formation of such three-dimensional network microstructure in Mg alloys. Finally, we note that the *in situ* testing-imaging methodology in the present work enables a fast screening of potential strengthening microstructures, and as such represents a step-forward in implementing the strategy prescribed in the "Materials Genome Initiative" for accelerating the design of high-performance alloys.

Acknowledgements

Z.W.S. and B.Y.L. acknowledge the supports by the National Key Research and Development Program of China (Nos. 2017YFB0702001), National Natural Science Foundation of China (Nos. 51601141, 51231005 and 51621063), and the Science and Technology Department of Shaanxi Province (Nos. 2016KTZDGY-04-03 and 2016KTZDGY-04-04). B.Y.L. thanks the support from the China Postdoctoral Science Foundation (2016M600788).

Appendix A. Supplementary data

Supplementary data associated with this article can be found, in the online version, at https://doi.org/10.1016/j.jmst.2018.01.017.

References

[1] X.J. Wang, D.K. Xu, R.Z. Wu, X.B. Chen, Q.M. Peng, L. Jin, Y.C. Xin, Z.Q. Zhang, Y. Liu, X.H. Chen, G. Chen, K.K. Deng, H.Y. Wang, J. Mater, Sci. Technol. (2017), http://dx.doi.org/10.1016/j.jmst.2017.07.019.
[2] W.J. Joost, P.E. Krajewski, Scr. Mater. 128 (2017) 107–112.
[3] S.P. Ringer, K. Hono, Mater. Charact. 44 (2000) 101–131.
[4] J.F. Nie, Metall. Mater. Trans. A 43 (2012) 3891–3939.
[5] E.W. Kelley, W.F. Hosford, Trans. Metall. Soc. AIME 242 (1968) 5–13.
[6] J.F. Nie, Scr. Mater. 48 (2003) 1009–1015.
[7] J.D. Robson, N. Stanford, M.R. Barnett, Acta Mater. 59 (2011) 1945–1956.
[8] P. Hidalgo-Manrique, J.D. Robson, M.T. Pérez-Prado, Acta Mater. 124 (2017) 456–467.
[9] N. Stanford, M.R. Barnett, Mater. Sci. Eng. A 516 (2009) 226–234.
[10] S.R. Agnew, R.P. Mulay, F.J. Polesak, C.A. Calhoun, J.J. Bhattacharyya, B. Clausen, Acta Mater. 61 (2013) 3769–3780.
[11] J.T. Wang, N. Stanford, Acta Mater. 100 (2015) 53–63.
[12] J. Jain, P. Cizek, W.J. Poole, M.R. Barnett, Mater. Sci. Eng. A 647 (2015) 66–73.
[13] S.R. Kada, P.A. Lynch, J.A. Kimpton, M.R. Barnett, Acta Mater. 119 (2016) 145–156.
[14] M. Lentz, M. Klaus, M. Wagner, C. Fahrenson, I.J. Beyerlein, M. Zecevic, W. Reimers, M. Knezevic, Mater. Sci. Eng. A 628 (2015) 396–409.
[15] N. Stanford, J. Geng, Y.B. Chun, C.H.J. Davies, J.F. Nie, M.R. Barnett, Acta Mater. 60 (2012) 218–228.
[16] J.B. Clark, Acta Metall. 16 (1968) 141–152.

[17] M.A. Gharghouri, G.C. Weatherly, J.D. Embury, Philos. Mag. A 78 (1998) 1137–1149.
[18] J. Robson, N. Stanford, M. Barnett, Metall. Mater. Trans. A 44 (2013) 2984–2995.
[19] M. Matsuda, S. Ii, Y. Kawamura, Y. Ikuhara, M. Nishida, Mater. Sci. Eng. A 386 (2004) 447–452.
[20] J.D. Robson, Acta Mater. 121 (2016) 277–287.
[21] M.R. Barnett, Mater. Sci. Eng. A 464 (2007) 1–7.
[22] B.Y. Liu, J. Wang, B. Li, L. Lu, X.Y. Zhang, Z.W. Shan, J. Li, C.L. Jia, J. Sun, E. Ma, Nat. Commun. 5 (2014) 3297.
[23] B.-Y. Liu, L. Wan, J. Wang, E. Ma, Z.-W. Shan, Scr. Mater. 100 (2015) 86–89.
[24] Q. Zu, X.-Z. Tang, S. Xu, Y.-F. Guo, Acta Mater. 130 (2017) 310–318.
[25] C.D. Barrett, H. El Kadiri, Acta Mater. 63 (2014) 1–15.
[26] P.G. Partridge, E. Roberts, Acta Metall. 12 (1964) 1205–1210.
[27] X.Y. Zhang, B. Li, X.L. Wu, Y.T. Zhu, Q. Ma, Q. Liu, P.T. Wang, M.F. Horstemeyer, Scr. Mater. 67 (2012) 862–865.
[28] J. Wang, L. Liu, C.N. Tomé, S.X. Mao, S.K. Gong, Mater. Res. Lett. 1 (2013) 81–88.
[29] J. Geng, Y.B. Chun, N. Stanford, C.H.J. Davies, J.F. Nie, M.R. Barnett, Mater. Sci. Eng. A 528 (2011) 3659–3665.
[30] X.H. Shao, S.J. Zheng, D. Chen, Q.Q. Jin, Z.Z. Peng, X.L. Ma, Sci. Rep. 6 (2016) 30096.
[31] J. Xu, B. Guan, H. Yu, X. Cao, Y. Xin, Q. Liu, J. Mater. Sci. Technol. 32 (2016) 1239–1244.
[32] M.D. Uchic, D.M. Dimiduk, J.N. Florando, W.D. Nix, Science 305 (2004) 986–989.
[33] G. Li, J. Zhang, R. Wu, Y. Feng, S. Liu, X. Wang, Y. Jiao, Q. Yang, J. Meng, J. Mater, Sci. Technol. (2017), http://dx.doi.org/10.1016/j.jmst.2017.12.011, in press.
[34] N. Stanford, R.K.W. Marceau, M.R. Barnett, Acta Mater. 82 (2015) 447–456.
[35] J.J. Bhattacharyya, F. Wang, P.D. Wu, W.R. Whittington, H.E. Kadiri, S.R. Agnew, Int. J. Plast. 81 (2016) 123–151.
[36] J.F. Nie, Y.M. Zhu, J.Z. Liu, X.Y. Fang, Science 340 (2013) 957–960.
[37] Z. Xu, M. Weyland, J.F. Nie, Acta Mater. 75 (2014) 122–133.
[38] Q. Yu, Z.-W. Shan, J. Li, X. Huang, L. Xiao, J. Sun, E. Ma, Nature 463 (2010) 335–338.
[39] M. Nishijima, K. Hiraga, M. Yamasaki, Y. Kawamura, Mater. Trans. 50 (2009) 1747–1752.
[40] H. Liu, Y. Gao, Z. Xu, Y.M. Zhu, Y. Wang, J.F. Nie, Sci. Rep. 5 (2015) 16530.

Supplementary Material

Insight from in situ microscopy into which precipitate morphology can enable high strength in magnesium alloys

Bo-Yu Liu [a], Nan Yang [a], Jian Wang [b], Matthew Barnett [c], Yun-Chang Xin [d], Di Wu [e], Ren-Long Xin [d], Bin Li [f], R. Lakshmi Narayan [a, g], Jian-Feng Nie [h], Ju Li [a, i], Evan Ma [a, j, *], Zhi-Wei Shan [a, *]

[a] *Center for Advancing Materials Performance from the Nanoscale (CAMP-Nano) & Hysitron Applied Research Center in China (HARCC), State Key Laboratory for Mechanical Behavior of Materials, Xi'an Jiaotong University, Xi'an 710049, People's Republic of China.*

[b] *Mechanical and Materials Engineering, University of Nebraska-Lincoln, Lincoln, NE 68588, USA*

[c] *Institute for Frontier Materials, Deakin University, Geelong, Victoria, 3216, Australia*

[d] *College of Materials Science and Engineering, Chongqing University, Chongqing, 400045, People's Republic of China*

[e] *Institute of Metal Research, Chinese Academy of Sciences, Shenyang 110016, People's Republic of China*

[f] *Department of Chemical and Materials Engineering, University of Nevada, Reno, USA*

[g] *Department of Materials Science and Engineering, Carnegie Mellon University, Pittsburgh, Pennsylvania 15213, USA*

[h] *Department of Materials Science and Engineering, Monash University, Melbourne, Vic, 3800, Australia*

[i] *Department of Nuclear Science and Engineering and Department of Materials Science and Engineering, Massachusetts Institute of Technology, 77 Massachusetts Avenue, Cambridge, MA 02139, USA*

[j] *Department of Materials Science and Engineering, Johns Hopkins University, Baltimore, Maryland 21218, USA*

E-mail address: zwshan@xjtu.edu.cn (Z.W. Shan); ema.mse.jhu@gmail.com (E. Ma).

Specimen sources. (*i*) The AZ31 alloy (Mg - 2.75wt.% Al - 0.64wt.% Zn - 0.27wt.% Mn) was provided by Prof. Y.C. Xin at Chongqing University. The sample was obtained from a hot rolled sheet and aged at 100 ℃ for 1 h. (*ii*) The ZK60 alloy (Mg - 6.2wt.% Zn - 0.5wt.% Zr) was provided by Prof. R.L. Xin at Chongqing University. The sample aged at 175 ℃ for 10 h. (*iii*) The Z6 alloy (Mg – 6wt.% Zn) was provided by Prof. M.R. Barnett at Deakin University. The sample aged at 200 ℃ for 8 h. (*iv*) The WE54 alloy (Mg - (5.0-5.5) wt.% Y - (1.5-2.0) wt.% Nd - (1.5-2) wt.% Heavy RE - 0.4 wt.% Zr) was provided by Prof. J.F.Nie at Monash University. The WE54 alloy plate was purchased from MEL, in the as-received condition of "solution treated at 525 °C for 8 hours, air cooled, and aged at 250 °C for 16 hours". Small blocks with a dimension of 10 × 5 × 20 mm were cut from the as-received plate and re-solution treated for 8 hours at 525 °C, water quenched and aged for 10 hours at 250 °C. (*v*) The GWZ931 alloy (Mg - 9.25wt.% Gd - 2.88wt.%Y - 0.46wt.%Zn - 0.39wt.% Zr) was provided by Prof. R.S. Chen at Institute of Metal Research, Chinese Academy of Sciences. The GWZ931 alloy was prepared from pure Mg (99.95 wt.%), Gd (99.5 wt.%), Y (99.5 wt.%), Zn (99.9 wt.%) and Mg-30Zr (wt.%) by melting the mixture in an electric resistance furnace, under protection of the RJ-6 anti-oxidizing flux, and pouring the melt into a preheated steel mold. After homogenization at 500℃ for 16 h, the billet was extruded at 480℃ (extrusion ratio ~ 15:1). The thickness and interlayer spacing of the LPSO layers of this GWZ931 alloy are in the range of 6 - 15 nm and 20 - 110 nm, respectively.

Sample fabrication. The bulk samples were first cut into millimeter-sized pieces using wire-cut electrical discharge machining and ground into thin slices with a thickness of 100~200 micrometers. After that, a thin edge on the slice was made by twin-jet electro-polishing. Next, micron-sized plates were fabricated by using Focus Ion Beam (FIB) milling on this thin edge. Afterwards, the plates were transported to TEM to survey target regions containing precipitates or LPSO layers with appropriate size, spacing and amount. Then the sub-micron sized pillars were finally fabricated in such regions using FIB. In order to minimize the FIB damage, all pillars were made via glancing cutting on the lateral surface under low accelerating voltage (15 keV) and low ion current (several to tens of pA). The surfaces of the pillars were then cleaned under a low energy (5 keV) ion beam to remove

damaged layers. All pillars were designed to have a square cross-section to avoid tapering along the axial direction. The width and length of each pillar was ~400 nm and1.3~1.6 μm, respectively.

Imaging. All in-situ testing and characterizations were conducted inside a JEOL 2100FEG TEM (200 keV). In bright field or dark field TEM images and in-situ videos, due to the higher mass of Al, Mn, Zn, Zr, Gd, Y atoms than Mg atoms, the Al_8Mn_5 particles, Zn-rich particles/rods/nanoplates, and LPSO layers exhibit darker contrast compared to that of the Mg matrix. During mechanical loading, the imaging condition may be disturbed by the plastic deformation or strain burst occurring in the sample, which changes the diffraction contrast. But the general features of twin boundaries, precipitates and LPSO layers can still be readily followed. Bright-field STEM imaging was also used to clearly observe the shape and location of the particles, rods, plates, and the LPSO layers, all of which have a darker Z-contrast compared to that of the Mg matrix. Moreover, the LPSO layers can also be observed using dark-field imaging in the TEM due to its different crystal structure from that of the Mg matrix.

In-situ testing. All in-situ quantitative mechanical tests were carried out using a Hysitron PicoIndenter (PI95). Compression loading was conducted under a constant displacement rate of 5 $nm \cdot s^{-1}$ or 10 $nm \cdot s^{-1}$. As the pillar length was in the range of 1.3~1.6 μm, the strain rate was of the order of 10^{-3} s^{-1}, which is a typical quasi-static condition. During the mechanical loading, the microstructure evolution was recorded using a GATAN 833 camera. The in-situ movies and the corresponding synchronized stress-strain curves were then combined, as shown in the Supplementary videos 1 – 6. In the right column of the video, the latest region of the stress-strain curve is magnified and displayed as the upper curve to observe more details.

Microstructure evolution and corresponding mechanical response. ***Supplementary video 1***. The ZK60 pillar was compressed along $[0\bar{1}10]$ (parallel to the basal plane). At ~330 MPa, a narrow twin nucleus formed at the top-right corner of the pillar. After dwelling at that position for a short while, the twin propagated to the left surface of the pillar when the stress increased to ~350 MPa. At the same instant, the stress-strain curve developed a stain burst of ~1.3% along with a stress drop. When the stress exceeded ~360 MPa, the lower boundary started to migrate towards the root of the

pillar in a stick-slip/jerky manner. Each jump of the lower boundary was manifested in the stress-strain behavior as a strain burst and a stress drop. ***Supplementary video 2***. The Z6 pillar was compressed in the direction parallel to the basal plane. The twin formed at the stress of ~300 MPa, accompanied by a corresponding strain burst and stress drop. After the stress reached ~400 MPa, the twin boundary started jerky migration downwards. Each jump of the twin boundary resulted in a strain burst and a stress drop. After the entire pillar got twinned, continued loading caused a remarkable increase of the measured stress, reminiscent of the concave-down stress-strain curve in testing bulk Mg alloy samples along the twinning favored orientation. ***Supplementary video 3***. The WE54 pillar with two precipitate plates was compressed along $[0\bar{1}10]$. The pillar yields at ~350 MPa. A small twin was formed at the right-top corner of the pillar when the stress achieved at ~500 MPa. At that time, the engineering strain was ~8%. After that, the twin gradually grew towards the root part of the pillar. In this process, no obvious strain burst or stress drop could be observed, indicating a smooth growth of this twin. At last, this twin stopped at the location of a precipitate plate. Continued loading caused stress increasing. ***Supplementary video 4***. The WE54 pillar with plate-networks was compressed along $[0\bar{1}10]$. This pillar yields at ~350 MPa. After an obvious strain-hardening stage, the peak stress of ~600 MPa was reached. When the engineering strain reached ~12%, one precipitate plate was observed to be sheared. This may correspond to the slight decrease of flow stress. After compression test, no twin could be detected in this pillar despite of the obvious plastic deformation. ***Supplementary video 5***. The GWZ931-a pillar containing about four LPSO layers was compressed along the direction parallel to the basal plane. When the stress reached ~500 MPa, a twin formed with a large strain burst of ~2%. The measured stress dropped to ~100 MPa. After the stress rose back up to ~500 MPa again, the twin boundary started to smoothly migrate until it approached the root part of the pillar. At the strain of ~8%, the diamond punch was retracted. During unloading, the twin boundary started to move back when the compressive stress remained at ~ 200 MPa. Such de-twinning process led to a deviation of the unloading stress-strain curve from linearity. ***Supplementary video 6***. The GWZ931-b pillar containing about 10 LPSO layers was also compressed along the basal plane. The pillar yielded at ~ 600 MPa, although no twins formed at this instant. After some strain hardening, possibly due to dislocation accumulation, the stress increased to

700 MPa, at which point a narrow twin nucleated at the top-right corner of the pillar. However, the twin front did not propagate further. When the plastic strain reached ~4%, another twin formed at the top-left corner of the pillar. On further loading, it appeared that the twin propagated through several lamellae and reached the right edge of the pillar. But after carefully observing the twins, their boundary profiles were found to be discontinuous at the LPSO layers. A small protruding feature, highlighted with a white arrow in Fig. 4b, also lends evidence to this notion of a discontinuous twin boundary.

Strain-component analysis. The proportion of $\varepsilon_{elastic}$, $\varepsilon_{dislocation}$ and ε_{twin} in the ε_{total} is calculated by the following procedures. Sample points are selected from the stress-strain curve. (1) $\varepsilon_{elastic} = \sigma/S$, where σ is the flow stress, S is the slope obtained from the linear region in stress-strain curve. (2) $\varepsilon_{twin} = \nu_{twin} \times 6.3\%$, where ν_{twin} is the twin volume fraction at the selected moment, *6.3%* is the plastic strain produced by $\{10\bar{1}2\}$ deformation twin along the c-axis. Because the image acquired by TEM is a two-dimensional projection, the volume (area × thickness) fraction was approximated by the "area fraction", $\nu_{twin}=area_{twin}/area_{pillar}$. The twinned area in each sample was measured on the snapshot captured from in-situ movie. Because the twin boundary usually had irregular morphology in 3D space rather than strictly following the twinning plane, the twin boundary often appeared fuzzy in the snapshot, leading to an error margin in measuring the twinned area. (3) $\varepsilon_{dislocation} = \varepsilon_{total} - \varepsilon_{elastic} - \varepsilon_{twin}$. Then the diagram of strain-components *vs.* engineering strain (ε_{total}) is plotted by using "area stacked" mode with different colors. The corresponding flow stresses are overlapped on the strain-component diagram. Original data for strain-component analysis are shown in Tables S2 – S8.

Supplementary Figures

Figure S1 The effect of age-hardening in Mg alloys and Al alloys. Data are collected from Ref.[1-27].

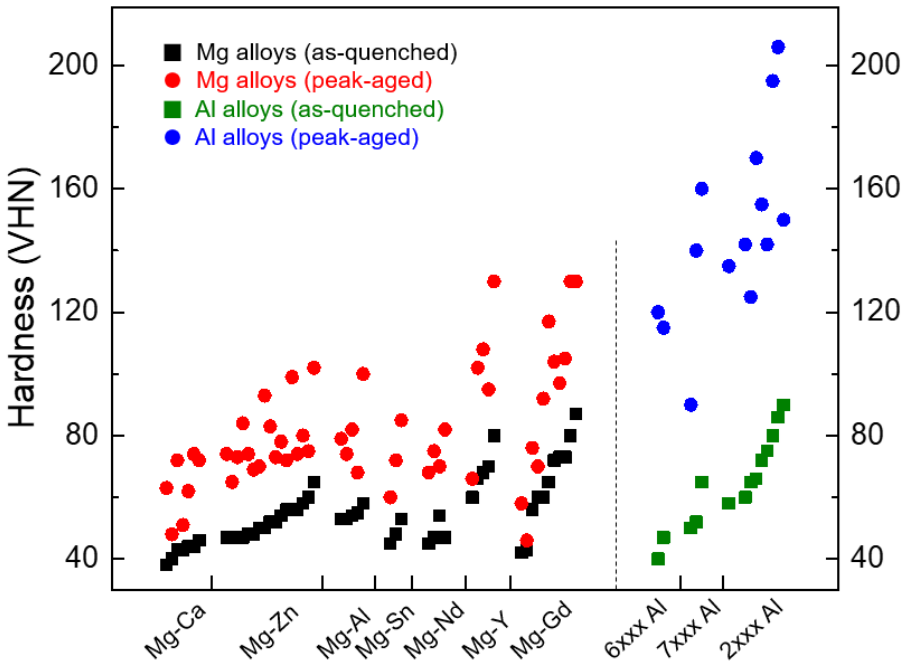

Figure S2 Schematic stress-strain curves illustrating the deformation anisotropy of Mg when stretched or compressed along different crystal orientations.

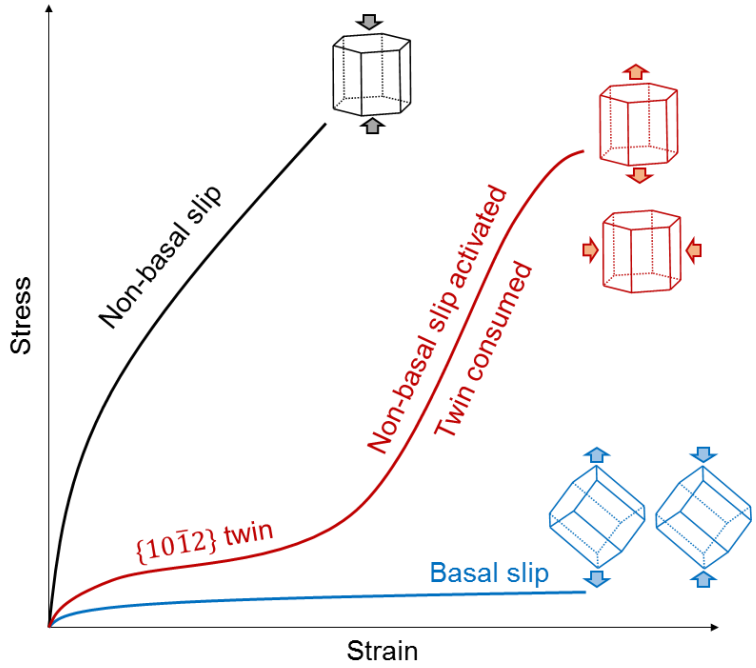

Figure S3 Possible activated plasticity modes in Mg when compressed along $\langle 10\bar{1}0\rangle$ (perpendicular to prismatic plane). (a) $\{10\bar{1}2\}$ twinning or prismatic-basal transformation, providing c-axis elongation. **(b)** prismatic ***a*** slip, no c-axis strain but fattening in the direction perpendicular to the loading axis. **(c)** ***c+a*** slips on pyramidal I or pyramidal II planes, providing c-axis elongation.

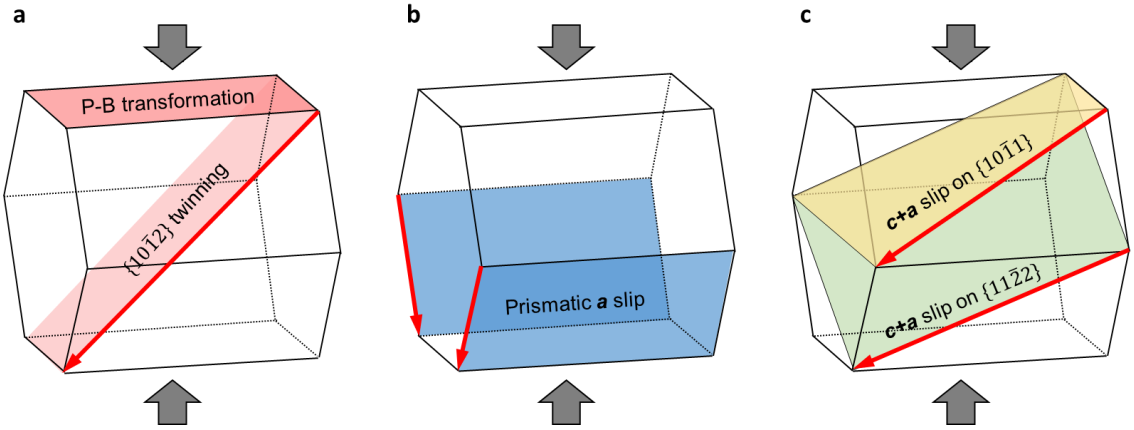

Figure S4 Stress-strain curve and snapshots from the in-situ TEM video of a compression test on a pure Mg pillar. Twinned area was outlined using white dashed frame.

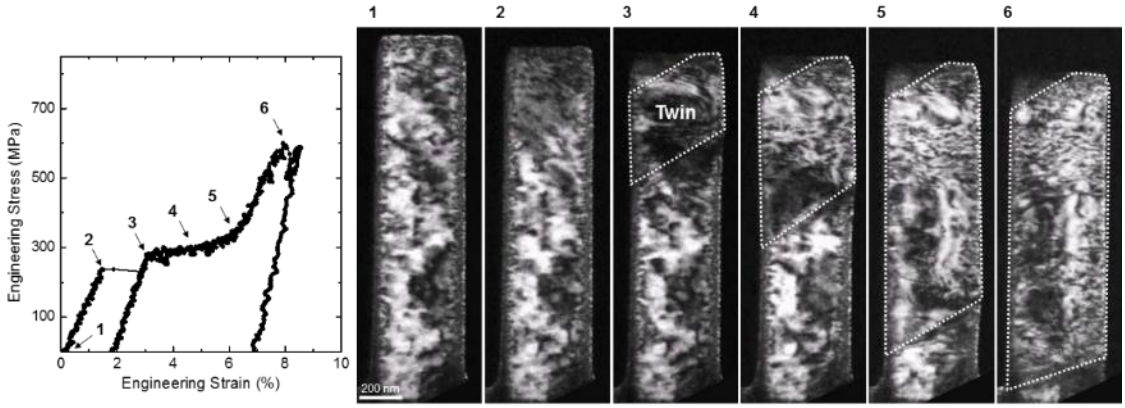

Figure S5 In-situ compression test on AZ31 pillar with Al8Mn5 particles. (a) Chemical analysis of a particle in another AZ31 sample. The energy dispersive spectrum (EDS) spot scan indicating that the particle was mainly composed of Al and Mn. Quantitative analysis showed Al/Mn ratio (atom%) was 1.58, agreeing well with the stoichiometry of Al8Mn5. The strong Mg signal rose from the Mg matrix. Scale bar, 200 nm. **(b)** Stress-strain curve and snapshots from the in-situ TEM video. Twinned area was outlined by white dashed frame.

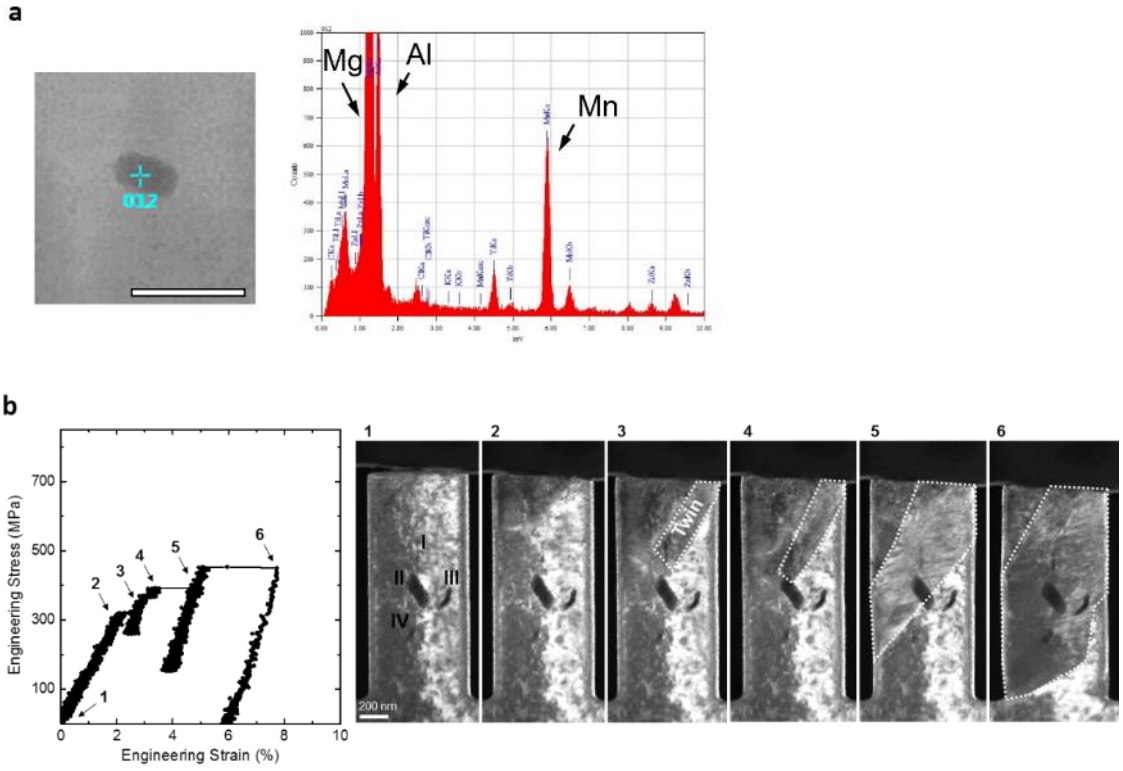

Figure S6 In-situ compression test on Mg-Zn alloy pillars. (a) Chemical analyses of the precipitates in a ZK60 sample. The EDS spot scan and mapping indicating the enrichment of Zn and Zr at the precipitates. **(b)** Stress-strain curve and snapshots from the in-situ TEM video of a compression test on sub-micron sized ZK60 pillar with dense particulate precipitates. **(c)** Z6 pillar with dense rod shaped precipitates and a few nanoplates. Twinned area was outlined by white dashed frame. Insets: diffraction patterns showing the $\{10\bar{1}2\}$ twin relation. The (0002) spots in matrix and twin (yellow circle) demonstrate the ~90° reorientation of the c-axis.

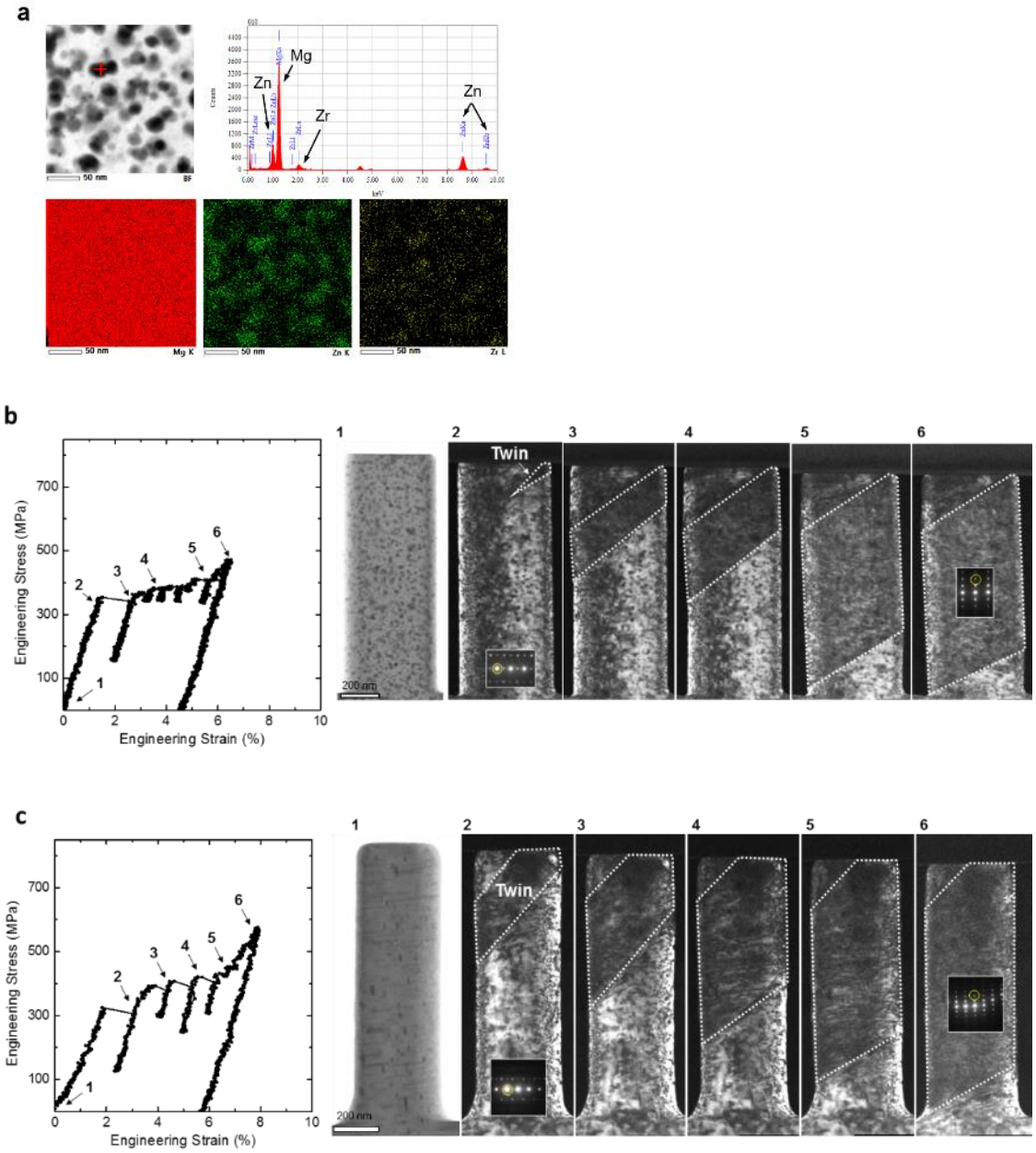

Figure S7 In-situ compression test on WE54 pillars. (a) Stress-strain curve and snapshots from the in-situ TEM video of a compression test on sub-micron sized WE54 pillar with two prismatic plates. Insets: diffraction patterns showing the $\{10\bar{1}2\}$ twinning relation. Twinned area was outlined by white dashed frame. **(b)** WE54 pillar with plate-networks. No twin can be observed in the deformed sample. Insets, diffraction patterns showing no DT. **(c)-(d)** Strain component analyses of compression tests in (a) and (b). (e) SEM image of the precipitate morphology in WE54 sample. Pillar in (a) was made from the area where prismatic plate does not connect to network. Pillar in (b) was made from area where plate-network formed.

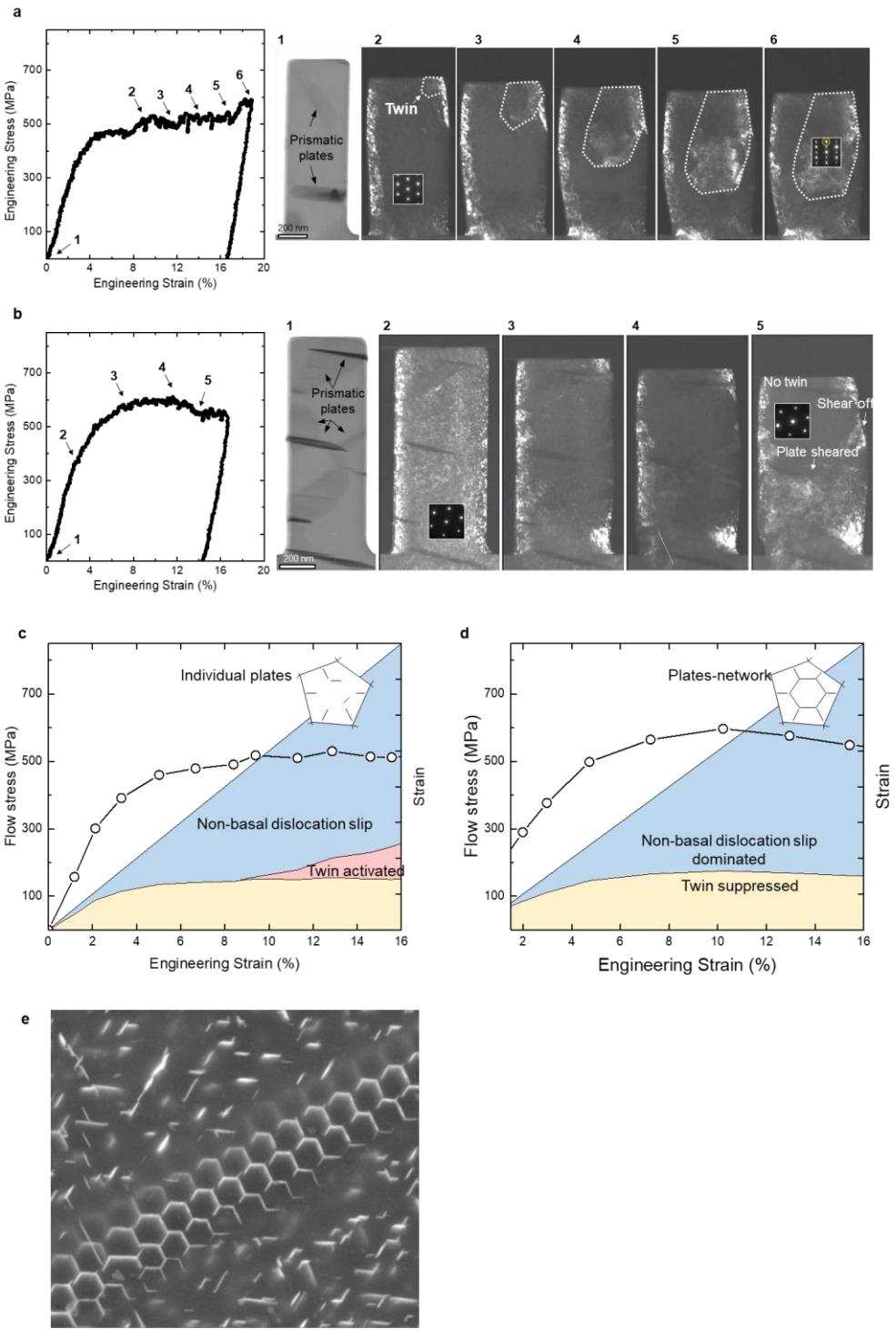

Figure S8 In-situ compression test on GWZ931 pillars. (a) Stress-strain curve and snapshots from the in-situ TEM video of a compression test on sub-micron sized GWZ931 pillar with a few LPSO lamellae (dark stripes). A single twin formed and expanded to the root part of the pillar. **(b)** GWZ931 pillar with more LPSO lamellae. Only two small twines formed in the top part of the pillar. **(c)-(d)** Strain component analyses of compression tests in (a) and (b). **(e)** EDS mapping on a GWZ931 sample showing the concentration of Gd, Y and Zn at the LPSO lamellae, respectively.

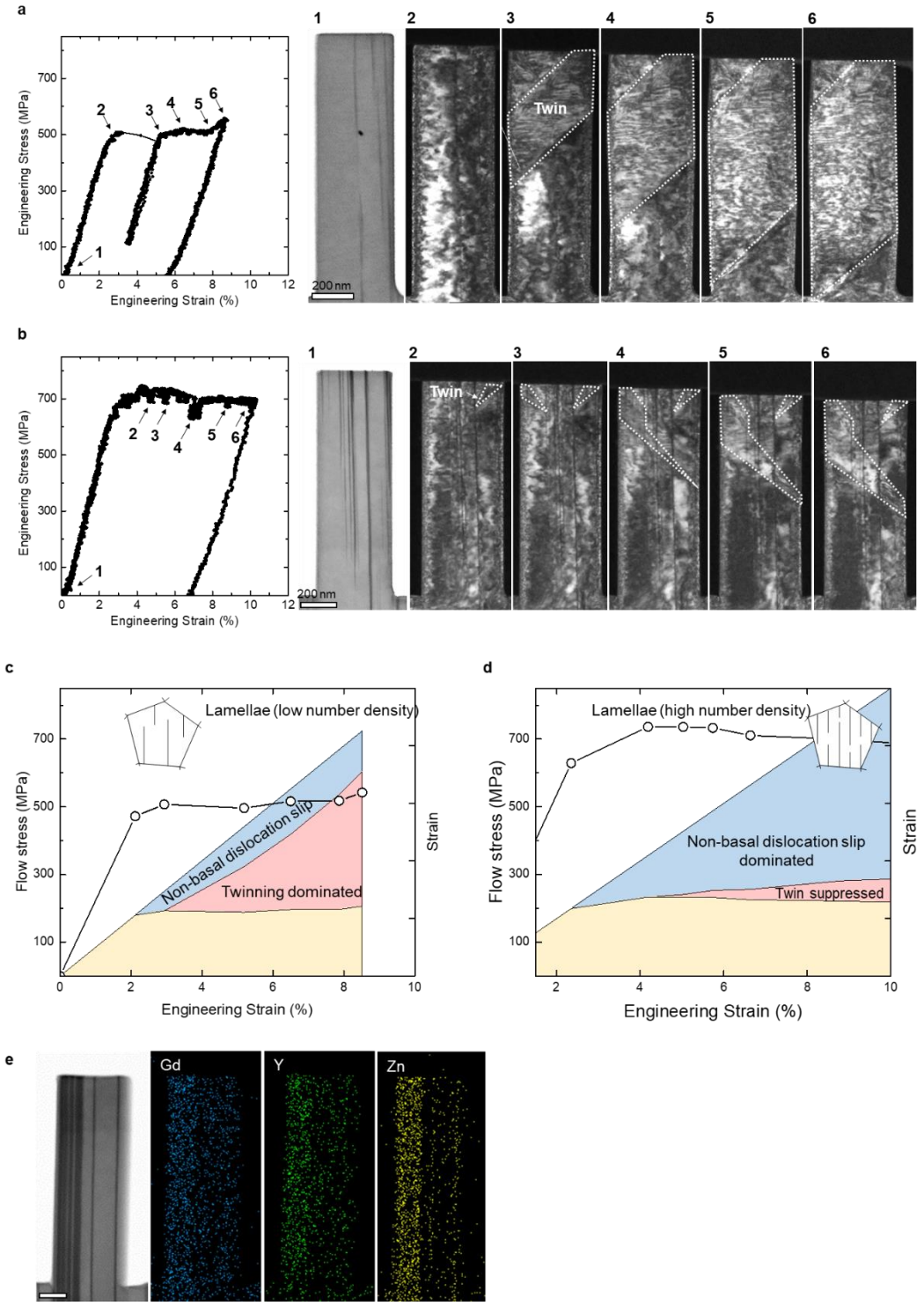

Figure S9 (a)-(d) A general trend that the thicker and denser the LPSO lamellae contained in a GWZ931 pillar, the less the $\{10\bar{1}2\}$ twin being activated. The up row are bright field STEM images showing the distribution of LPSO lamellae. The volume fraction of LPSO lamellae (Vf_{LPSO}) is measured from the approximation of an "area fraction" of dark streaks to the total pillar projection. The result is labeled in each panel. The bottom row are dark field TEM images showing the deformed pillars. Twin region is approximately outlined by dashed line. Insets are DPs to confirm the occurrence or suppression of $\{10\bar{1}2\}$ DT. Scale bars, 200 nm. **(e)** The corresponding stress-displacement curves.

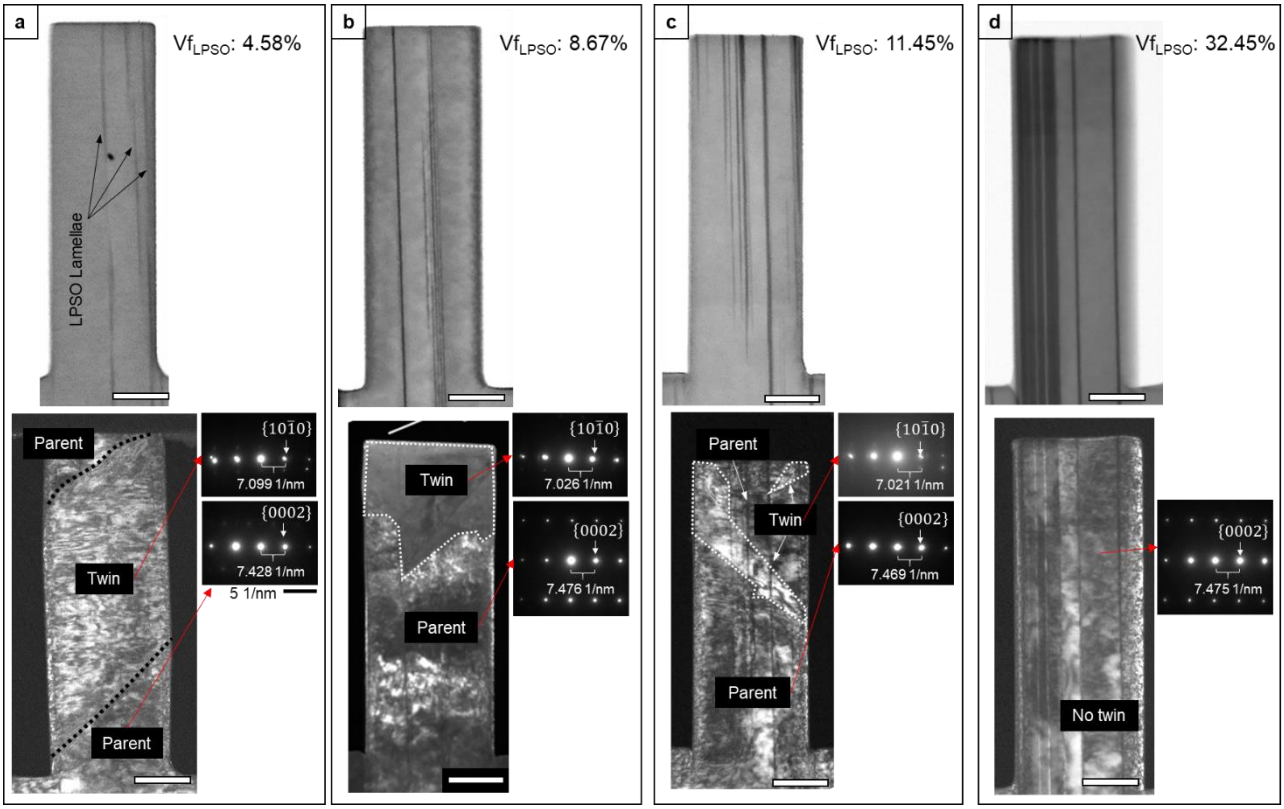

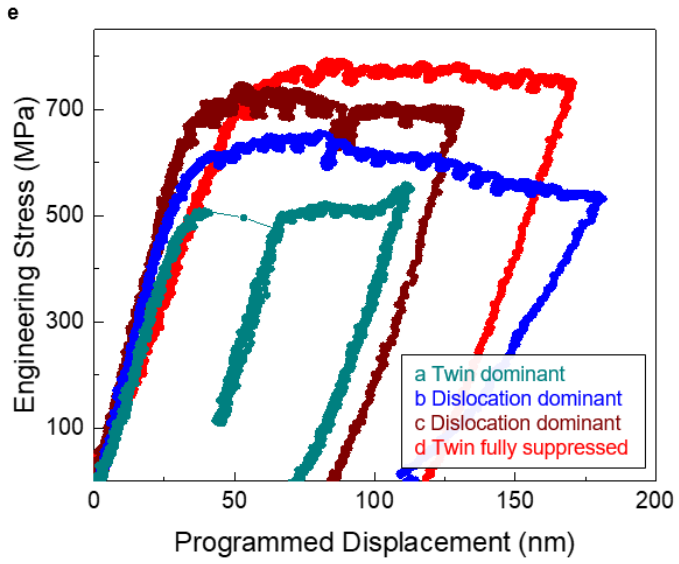

Figure S10 Strain-component analysis on pure Mg pillar. The loading direction is parallel to basal plane.

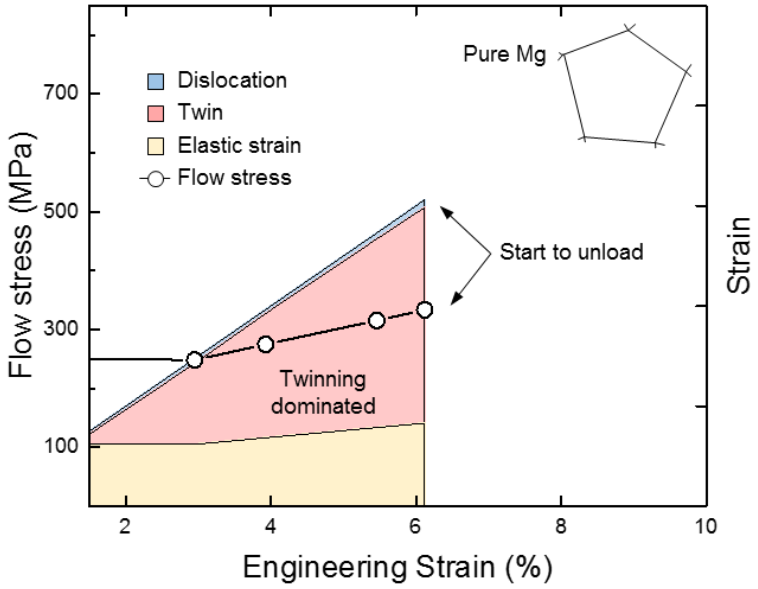

Supplementary Tables

Table S1 Summary of the experimental measurement of the change of stress required for $\{10\bar{1}2\}$ DT ($\Delta\tau$), twin volume fraction (ΔV_f), yield strength (ΔYS) and ultimate strength (ΔUS) in peak-aged samples compared to solutionized samples in several Mg alloys when loaded along the DT favorable orientation. Increased (↑), unchanged (→), decreased (↓), unreported (-).

#	Material	Precipitates	$\Delta\tau$	ΔV_f	ΔYS	ΔUS	Ref.
1	Mg-Y-Nd-Zr (WE43)	prismatic-plates	0 MPa	↑	90 MPa	75 MPa	[28]
2	Mg-Y-Nd-Zr (WE54)	prismatic-plates	0 MPa (250°C 16 h)	↑	-	-	[29]
			-37 MPa (400°C 24 h)	↑	-	-	
3	Mg-6Zn (wt)	c-rods	1 MPa	-	4 MPa	68 MPa	[30]
4	Mg-6Zn (wt)	c-rods	29 MPa	→	63 MPa	40 MPa	[31]
5	Mg-5Zn (wt)	c-rods	62 MPa	↓	88 MPa	22 MPa	[32]
6	Mg-9Al-1Zn (wt) (AZ91)	basal-plates	36 MPa	→	55 MPa	-	[33]
7	Mg-9Al-1Zn (wt) (AZ91)	basal-plates	20 MPa	-	50 MPa	-	[34]

Table S2 Data for strain-component analysis of the ZK60 pillar in Fig. 4(a).

Sample points	Flow stress (MPa)	ε_{total} (%)	$\varepsilon_{elastic}$ (%)	v_{twin} (%)	ε_{twin} (%)	$\varepsilon_{dislocation}$ (%)
1	0	0	0	0	0	0
2	350.96	1.55	1.39752	1.13	0.07119	0.08129
3	356.58	2.97	1.4199	20.88	1.31544	0.23466
4	378.38	3.95	1.50671	33.9	2.1357	0.30759
5	397.3	5.21	1.58205	55.25	3.48075	0.1472
6	425.58	6.06	1.69466	68.43	4.31109	0.05425
7	463.95	6.54	1.84745	72.73	4.58199	0.11056

Table S3 Data for strain-component analysis of the Z6 pillar in Fig. 4(b).

Sample points	Flow stress (MPa)	ε_{total} (%)	$\varepsilon_{elastic}$ (%)	v_{twin} (%)	ε_{twin} (%)	$\varepsilon_{dislocation}$ (%)
1	0	0	0	0	0	0
2	321.28	1.89	1.71532	0	0	0.17468
3	335.99	3.51	1.79386	15.77	0.99351	0.72263
4	358.35	4.58	1.91324	32.48	2.04624	0.62052
5	405.29	5.64	2.16385	49.13	3.09519	0.38096
6	423.74	6.88	2.26236	67.28	4.23864	0.379
7	557.86	8.12	2.97843	79.78	5.02614	0.11543

Table S4 Data for strain-component analysis of the WE54 pillar in Fig. 4(c).

Sample points	Flow stress (MPa)	ε_{total} (%)	$\varepsilon_{elastic}$ (%)	v_{twin} (%)	ε_{twin} (%)	$\varepsilon_{dislocation}$ (%)
1	0	0	0	0	0	0

2	199.3	1.11	1.10031	0	0	0.00969
3	289.8	1.99	1.59996	0	0	0.39004
4	376.8	2.98	2.08027	0	0	0.89973
5	498.5	4.73	2.75217	0	0	1.97783
6	564.7	7.24	3.11765	0	0	4.12235
7	596.8	10.22	3.29487	0	0	6.92513
8	576	12.95	3.18004	0	0	9.76996
9	548.4	15.42	3.02766	0	0	12.39234
10	543	16.48	2.99785	0	0	13.48215

Table S5 Data for strain-component analysis of the GWZ931 pillar in Fig. 4(d).

Sample points	Flow stress (MPa)	ε_{total} (%)	$\varepsilon_{elastic}$ (%)	v_{twin} (%)	ε_{twin} (%)	$\varepsilon_{dislocation}$ (%)
1	0	0	0	0	0	0
2	628.83	2.35	2.34446	0	0	0.00554
3	736.22	4.19	2.74484	0	0	1.44516
4	735.73	5.03	2.74301	1.43	0.09009	2.1969
5	732.78	5.74	2.73201	3.84	0.24192	2.76607
6	710.55	6.64	2.64913	5.78	0.36414	3.62673
7	699.23	8.8	2.60693	11.12	0.70056	5.49251
8	688	10.12	2.56506	12.89	0.81207	6.74287

Table S6 Data for strain-component analysis of the WE54 pillar in Fig. S 7c

Sample points	Flow stress (MPa)	ε_{total} (%)	$\varepsilon_{elastic}$ (%)	v_{twin} (%)	ε_{twin} (%)	$\varepsilon_{dislocation}$ (%)
1	0	0	0	0	0	0
2	157	1.18	0.86678	0	0	0.31322
3	301	2.13	1.66179	0	0	0.46821
4	391	3.31	2.15867	0	0	1.15133
5	460	5.02	2.53961	0	0	2.48039
6	479	6.67	2.64451	0	0	4.02549
7	491	8.39	2.71076	0	0	5.67924
8	518	9.39	2.85982	1.6	0.1008	6.42938
9	510	11.29	2.81566	8.46	0.53298	7.94136
10	530	12.86	2.92608	17.32	1.09116	8.84276
11	514	14.6	2.83774	23.56	1.48428	10.27798
12	512	15.56	2.8267	28.84	1.81692	10.91638
13	517	16.37	2.8543	33.78	2.12814	11.38756
14	549	17.47	3.03097	40.13	2.52819	11.91084
15	573	18.35	3.16347	40.42	2.54646	12.64007

Table S7 Data for strain-component analysis of the GWZ931 pillar in Fig. S 8c.

Sample points	Flow stress (MPa)	ε_{total} (%)	$\varepsilon_{elastic}$ (%)	v_{twin} (%)	ε_{twin} (%)	$\varepsilon_{dislocation}$ (%)
1	0	0	0	0	0	0
2	472	2.12	2.11186	0	0	0.00814
3	507	2.94	2.26846	0	0	0.67154
4	496.09	5.19	2.21964	25.14	1.58382	1.38654
5	516.07	6.5	2.30904	41.5	2.6145	1.57646
6	517.55	7.87	2.31566	63.42	3.99546	1.55888
7	542	8.52	2.42506	74.52	4.69476	1.40018

Table S8 Data for strain-component analysis of the pure Mg pillar in Fig. S 10

Sample Points	Flow stress (MPa)	ε_{total} (%)	$\varepsilon_{elastic}$ (%)	v_{twin} (%)	ε_{twin} (%)	$\varepsilon_{dislocation}$ (%)
1	0	0	0	0	0	0
2	249.9	1.3	1.24403	0	0	0.05597
3	248.4	2.95	1.23656	26.95	1.617	0.09644
4	274.8	3.93	1.36798	41.36	2.4816	0.08042
5	315.4	5.46	1.57009	62.83	3.7698	0.12011
6	333.41	6.12	1.65975	71.8	4.308	0.15225

[1] J.F. Nie, Metall. Mater. Trans. A 43 (2012) 3891-3939.

[2] S. Celotto, Acta Mater. 48 (2000) 1775-1787.

[3] C.J. Bettles, P. Humble, J.F. Nie. *The effect of trace additions on the ageing behaviour of AZ91E*. Inst Materials (1997).

[4] J.B. Clark, Acta Metall. 13 (1965) 1281-1289.

[5] G. Mima, Y. Tanaka, T. Jpn. I. Met. 12 (1971) 76.

[6] L.Y. Wei, G.L. Dunlop, H. Westengen, Metall. Mater. Trans. A 26 (1995) 1705-1716.

[7] J. Geng, X. Gao, X.Y. Fang, J.F. Nie, Scr. Mater. 64 (2011) 506-509.

[8] J. Buha, Mater. Sci. Eng., A 491 (2008) 70-79.

[9] C.L. Mendis, K. Oh-ishi, Y. Kawamura, T. Honma, S. Kamado, K. Hono, Acta Mater. 57 (2009) 749-760.

[10] X. Gao, S.M. Zhu, B.C. Muddle, J.F. Nie, Scr. Mater. 53 (2005) 1321-1326.

[11] J. Jayaraj, C.L. Mendis, T. Ohkubo, K. Oh-ishi, K. Hono, Scr. Mater. 63 (2010) 831-834.

[12] T.T. Sasaki, K. Oh-ishi, T. Ohkubo, K. Hono, Mater. Sci. Eng. A 530 (2011) 1-8.

[13] R. Wilson, C.J. Bettles, B.C. Muddle, J.F. Nie. Precipitation hardening in Mg-3 wt%Nd(-Zn) casting alloys. In: *Magnesium Alloys 2003, Pts 1 and 2* (eds. Kojima Y, Aizawa T, Higashi K, Kamado S). Trans Tech Publications Ltd (2003).

[14] X. Gao, S.M. He, X.Q. Zeng, L.M. Peng, W.J. Ding, J.F. Nie, Mater. Sci. Eng. A 431 (2006) 322-327.

[15] S.M. He, X.Q. Zeng, L.M. Peng, X. Gao, J.F. Nie, W.J. Ding, J. Alloy. Compd. 421 (2006) 309-313.

[16] T. Honma, T. Ohkubo, S. Kamado, K. Hono, Acta Mater. 55 (2007) 4137-4150.

[17] J.F. Nie, X. Gao, S.M. Zhu, Scr. Mater. 53 (2005) 1049-1053.

[18] X. Gao, J.F. Nie, Scr. Mater. 58 (2008) 619-622.

[19] T. Sato, I. Takahashi, H. Tezuka, A. Kamio, J. Jpn. Inst. Light Met. 42 (1992) 804-809.

[20] Y.M. Zhu, A.J. Morton, J.F. Nie, Scr. Mater. 58 (2008) 525-528.

[21] C.L. Mendis, K. Oh-ishi, T. Ohkubo, K. Hono, Scr. Mater. 64 (2011) 137-140.

[22] T.T. Sasaki, T. Ohkubo, K. Hono, Scr. Mater. 61 (2009) 72-75.

[23] H.K. Hardy, J. Inst. Metals 80 (1952) 483-492.

[24] I.J. Polmear, R.J. Chester, Scr. Metall. 23 (1989) 1213-1217.

[25] S.P. Ringer, B.C. Muddle, I.J. Polmear, Metall. Mater. Trans. A 26 (1995) 1659-1671.

[26] S.P. Ringer, K. Hono, Mater. Charact. 44 (2000) 101-131.

[27] A.K. Gupta, D.J. Lloyd, S.A. Court, Mater. Sci. Eng. A 301 (2001) 140-146.

[28] S.R. Agnew, R.P. Mulay, F.J. Polesak, C.A. Calhoun, J.J. Bhattacharyya, B. Clausen, Acta Mater. 61 (2013) 3769-3780.

[29] M. Lentz, M. Klaus, M. Wagner, C. Fahrenson, I.J. Beyerlein, M. Zecevic, W. Reimers, M. Knezevic, Mater. Sci. Eng., A 628 (2015) 396-409.

[30] J.T. Wang, N. Stanford, Acta Mater. 100 (2015) 53-63.

[31] J. Jain, P. Cizek, W.J. Poole, M.R. Barnett, Mater. Sci. Eng. A 647 (2015) 66-73.

[32] N. Stanford, M.R. Barnett, Mater. Sci. Eng., A 516 (2009) 226-234.

[33] S.R. Kada, P.A. Lynch, J.A. Kimpton, M.R. Barnett, Acta Mater. 119 (2016) 145-156.

[34] N. Stanford, J. Geng, Y.B. Chun, C.H.J. Davies, J.F. Nie, M.R. Barnett, Acta Mater. 60 (2012)

218-228.